Role of grain-level chemo-mechanics in composite cathode degradation of solid-state lithium batteries

Chuanlai Liu, Franz Roters and Dierk Raabe

Max-Planck-Institut für Eisenforschung GmbH, Max-Planck-Str. 1, Düsseldorf, 40237, Germany.

*Corresponding author(s). E-mail(s): c.liu@mpie.de; d.raabe@mpie.de;

Abstract

Solid-state Li-ion batteries, utilizing Ni-rich oxide cathodes, hold promise for high-energy electrochemical storage. However, Li intercalation-induced dimensional changes can lead to crystal defect formation in these cathodes, and contact mechanics problems between cathode and solid electrolyte. Understanding the interplay between cathode microstructure, operating conditions, micromechanics of battery materials, and capacity decay remains a challenge. Here, we present a microstructure-sensitive chemo-mechanical model to study the impact of grain-level chemo-mechanics on the degradation of composite cathodes. We reveal that crystalline anisotropy, state-of-charge-dependent Li diffusion rates, and lattice dimension changes drive dislocation nucleation in cathodes and contact loss at the cathode/electrolyte interface. These dislocations induce large lattice strain and trigger oxygen loss and structural degradation preferentially near the surface area of cathode particles. Moreover, contact loss is caused by the micromechanics resulting from the crystalline anisotropy of cathodes and the mechanical properties of solid electrolytes, not just operating conditions. These findings highlight the significance of grain-level cathode microstructures in causing cracking, formation of crystal defects, and chemo-mechanical degradation of solid-state batteries.

1 Introduction

Ni-rich layered oxide cathodes can yield substantial increase in energy density of solid-state Li-ion batteries, but they suffer from contact loss, and irreversible layered-to-spinel or disordered rock-salt-like phase transition [1–8]. These structural degradation mechanisms have been mainly attributed to oxygen loss and out-of-plane

transition metal (TM) migration arising from cathode/electrolyte interfacial side reactions [3, 9–12]. Cathode particle surface modification or coating techniques could partially alleviate interfacial degradation [13–15], however, the effectiveness of these strategies has proven insufficient to mitigate structural degradation in the bulk of cathode materials [2, 4, 5, 16, 17]. This dilemma raises the suspicion that the electrochemical instability of the cathode/electrolyte interface may not be the main cause behind the progressive capacity degradation observed over cycling. One of the critical aspects of solid-state batteries is the stress response of their complex microstructure to large volume changes (strains) driven by Li intercalation.

For the layered oxide cathode, Li-ions intercalate into the host structure, creating a gradient in the lattice parameter and a concurrent non-uniform elastic strain and large volume change (7.8% dilatation in $LiNi_{0.8}Mn_{0.1}Co_{0.1}O_2$ (NMC811)). The high stress buildup resulting from Li transport and crystalline anisotropy inevitably leads to contact loss and the formation of crystal defects in cathodes, in particular dislocations and stacking faults [4, 6, 18–25], as sketched in Fig. 1. The appearance of crystal defects in ion-insertion materials can generate heterogeneous nanoscale lattice strain and modify the local bonding environment, for example, the number of covalent bonding partners for oxygen, as revealed by coherent X-ray diffraction and atomic-scale characterization [4–6, 18–20, 24]. The metal-oxygen decoordination owing to defects leads to significant change in the local electronic structure, and can even change the relative ordering of electronic states [4, 20, 26, 27]. Although the exact nature of the defect-induced bonding environment change is debated and may vary among different materials, such as Ni-rich and Li-rich layered oxides, the large lattice strain associated with crystal defects can markedly reduce the energy barriers to remove lattice oxygen and trigger Li/TM ion mixing [4, 20, 26–29]. Therefore, besides the electrochemical instability of the cathode/electrolyte interface, the continuous accumulation of crystal defects in cathode particles due to Li (de)intercalation over cycling acts as the primary driving force for aggravating oxygen loss and altering the structural stability.

The solid-state batteries must be able to operate within a wide range of charging and discharging times, ranging from ultra-fast pulses to slow discharging over the course of multiple days. The various compositional strains imposed by these different (dis)charging rates can significantly affect the evolution of grain-level stress and strain responses in composite cathodes. Key to solving the challenges of the cathode/-electrolyte interface and crystal defect formation in cathodes is a clear understanding of the chemo-mechanics of the composite cathodes across battery-relevant length scales and strain rates. High-resolution transmission electron microscopy (HRTEM) experiments and atomic-scale simulations reveal that dislocations resulting from heterogeneous Li intercalation can trigger irreversible migration of TM ions into octahedral sites in the Li layer and subsequent structural degradation [4–6, 18–20, 24, 27]. However, the assessment of how microstructure and (dis)charging protocols affect micromechanics and the formation of crystal defects in composite cathodes remains unexplored. This gap in knowledge is primarily due to the limitations and efforts associated with the application of advanced and standardized analytical techniques in probing cathodes and their environments across various length scales [4, 5]. In this work, we have therefore developed a meso-scale chemo-mechanical constitutive

model by integrating the interplay between electrochemical reaction, anisotropic Li-ion intercalation, cathode microstructure, grain-level micromechanics and formation of crystal defects resulting from lattice dimension changes [4, 5, 26, 27]. We apply it to systematically investigate the impact of cathode microstructure, mechanical properties of solid electrolyte, and operating conditions on the evolution of stress and strain responses, generation of dislocations, as well as the associated oxygen loss and structural degradation mechanisms. Our work provides insights into the impact of grain-level chemo-mechanics on the degradation of Ni-rich composite cathodes, aiming at providing a quantitative simulation methodology for mitigating capacity loss of solid-state batteries.

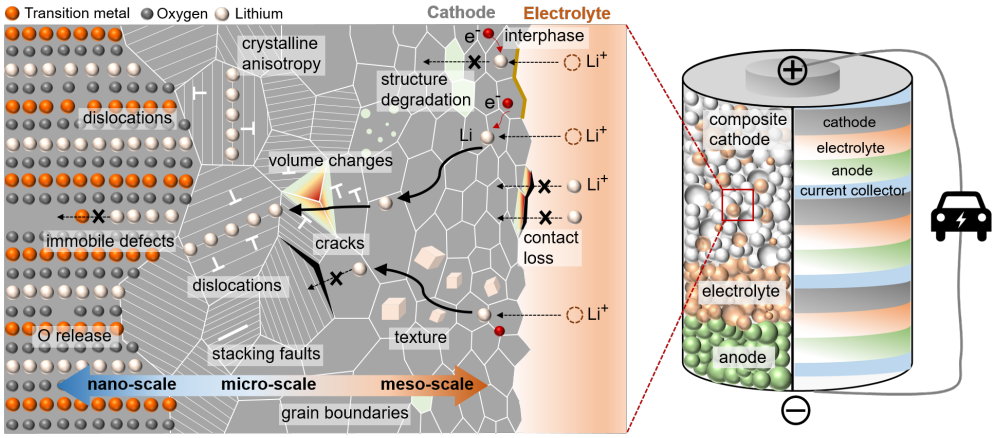

Fig. 1 Schematic view of electrochemical reaction, Li intercalation, structural degradation, and lattice defect types in composite cathodes of solid-state battery cells: point defects (zero-dimensional (0D) defects), dislocations (one-dimensional (1D) defects) and interfaces (two-dimensional(2D) defects). Key to solving the challenges of the cathode/electrolyte interface, crystal defect formation, and structural degradation in cathodes is a clear understanding of the chemo-mechanics of the composite cathodes across battery-relevant length scales. Non-uniform volume changes resulting from Li intercalation and the crystalline anisotropy of primary cathode particles lead to high stress, contact loss, and crystal defect accumulation, in particular dislocations and stacking faults. The presence of crystal defects can markedly reduce the energy barriers to remove lattice oxygen, which triggers Li/TM ion mixing and structural degradation. The large compositional strains in cathodes result in contact mechanics problems between cathodes and solid electrolyte.

2 Theoretical framework and model setup

The workflow of the electrochemical reaction-diffusion model and dislocation-based micromechanical model, informed by nanoscale experimental and theoretical findings [4, 5, 12, 16, 26, 27], is shown in Fig. 2. The procedure comprises three essential steps:

(1) A representative volume element is employed to describe the composite cathode microstructure, as shown in Fig. 2c. An isolated Ni-rich NMC811 polycrystal

particle with 200 primary particles is embedded in the uniform solid electrolyte. The solid-electrolyte is assumed to respond with isotropic mechanical properties. As characterized by electron backscatter diffraction measurements [30], the NMC811 polycrystalline secondary particles exhibit randomly distributed crystallographic orientations (Fig. 3b). The polycrystalline cathode particle maintains electrical neutrality as it is assumed to be connected to the current collector via the carbon binder of the composite cathode.

(2) A grain-level chemo-mechanical model is developed to describe the electrochemical reaction, Li intercalation, lattice dimension changes, and dislocation formation. The Cahn-Hilliard reaction-diffusion equation [31–33] is employed to describe the electrochemical reaction at the cathode/solid-electrolyte interface, and Li intercalation within the cathode. Li-ion transport inside the solid electrolyte is not considered explicitly since we only simulate discharge processes at constant current. The composite cathode is working under galvanostatic discharge conditions, *i.e.* a constant Li flux into the NMC secondary particle across the cathode/solid-electrolyte interface. For each primary particle within the secondary particle, the layered structure of the oxide cathode permits Li diffusion exclusively within the basal crystallographic plane, with diffusivity depending on the state-of-charge (Fig. 3c). To accommodate the anisotropic lattice dimension changes resulting from Li (de)intercalation, misfit dislocations in cathodes are usually generated (Fig. 2d,e), which is described by the crystal plasticity mechanical model [34, 35]. Only isotropic elastic deformation is allowed for the solid electrolyte.

(3) The impact of lattice strain resulting from dislocations on oxygen deficiency in the NMC cathode can be assessed via calculating the formation energy of oxygen vacancies under an applied mechanical strain [4, 26, 27] (Fig. 2f). The material domains with a plastic shear exceeding 12% in cathode particles after discharge are categorized as the oxygen-deficient phase. The formation of such an oxygen-deficient phase in cathode particles will impede the Li-ion intercalation pathways within the cathodes for the subsequent cycling. The Methods section and Supplementary Information provide more details on the full set of governing equations and model parameterization.

3 Crystalline anisotropy and kinetics for Li intercalation

We now investigate the role of crystalline anisotropy and concentration-dependent Li diffusivity in Li-ion dynamics, dislocation formation, mechanical failure, and capacity loss in composite cathode materials. A Ni-rich NMC811 polycrystal particle with a diameter of 12 μm is embedded in the $Li_{6.6}La_3Ta_{0.4}Zr_{1.6}O_{12}$ solid electrolyte. The composite cathode is working under the galvanostatic discharge condition, *i.e.* a constant Li flux into the NMC secondary particle. Three types of simulations are performed: (i) isotropic and (ii) anisotropic Li diffusion inside the primary particle, respectively, with a constant Li diffusivity, and (iii) anisotropic diffusion with a Li concentration-dependent diffusion coefficient. As demonstrated by solid-state nuclear magnetic resonance characterization, the Li diffusion coefficient drops sharply, over two orders of magnitude, as the Li content exceeds 80%. [36, 37] (Fig. 3c).

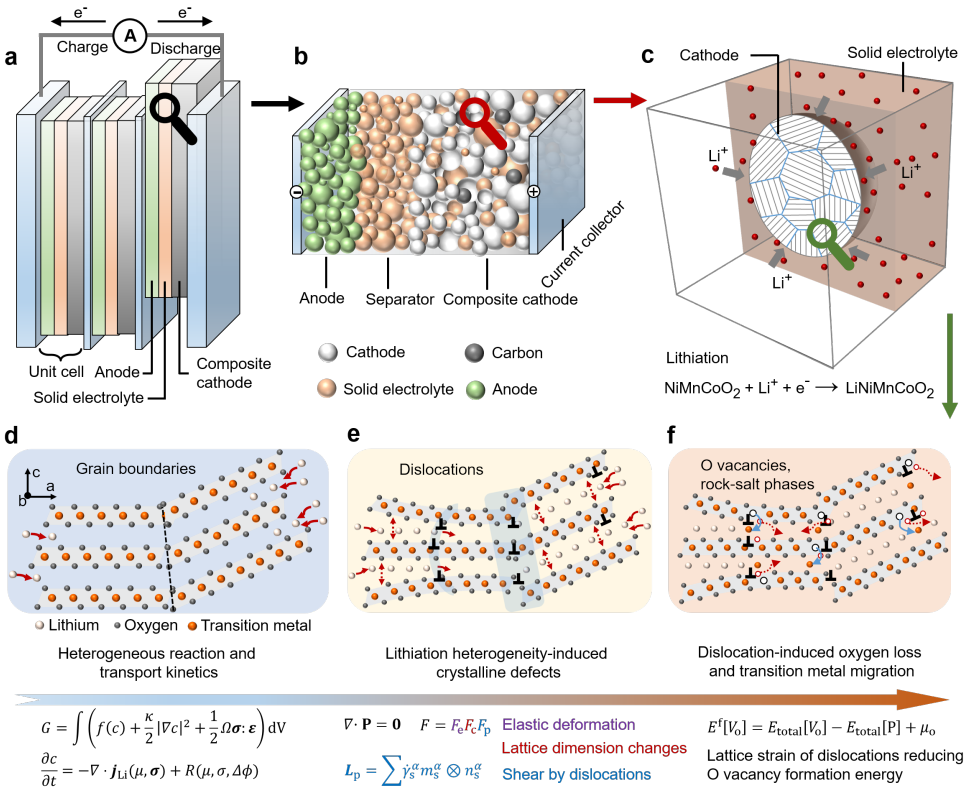

Fig. 2 Workflow of the reaction-diffusion-micromechanics and dislocation-induced structural degradation model for composite cathode materials, informed by nanoscale experimental and theoretical findings. a, Concept of a bipolar-stacked Li solid-state battery cell. **b**, Schematic of a unit cell featuring composite cathode materials. **c**, Representative volume element describing the microstructure of composite cathodes. **d**, Application of a Cahn-Hilliard diffusion-reaction model to describe the electro-chemical reactions and Li (de)intercalation in the a-b plane. **e**, Generation of various crystal defects, such as basal dislocations, arising from the anisotropic lattice dimension changes due to Li (de)intercalation. The coupling of Li composition and dislocation generation is described by a micromechanical constitutive law. **f**, The presence of dislocations resulting from Li mass transport facilitates oxygen removal and Li/TM ion mixing.

Fig. 3a-c,f show that anisotropic diffusion and state-of-charge dependent diffusivity result in secondary particles with Li-rich peripheries and Li-poor cores upon lithiation. This heterogeneous Li distribution is insufficient to enable a high Li-ion flux uniformly throughout the particle, thereby leading to a significant increase in over-potential and a consequent sharp reduction in cell voltage during galvanostatic discharge. Therefore, as shown in Fig. 3d, the half cell rapidly approaches the cut-off voltage of 3V, with the inner core of the particle remaining in a Li-deficient state, resulting in a substantial capacity loss. Fig. 3e and Supplementary Fig. S.5 demonstrate that the capacity loss arising from anisotropic diffusion increases from 3% to 17% as the discharge rate is raised from 0.25 C to 2 C (as quantified by the so-called C-rate, nC signifies to a full

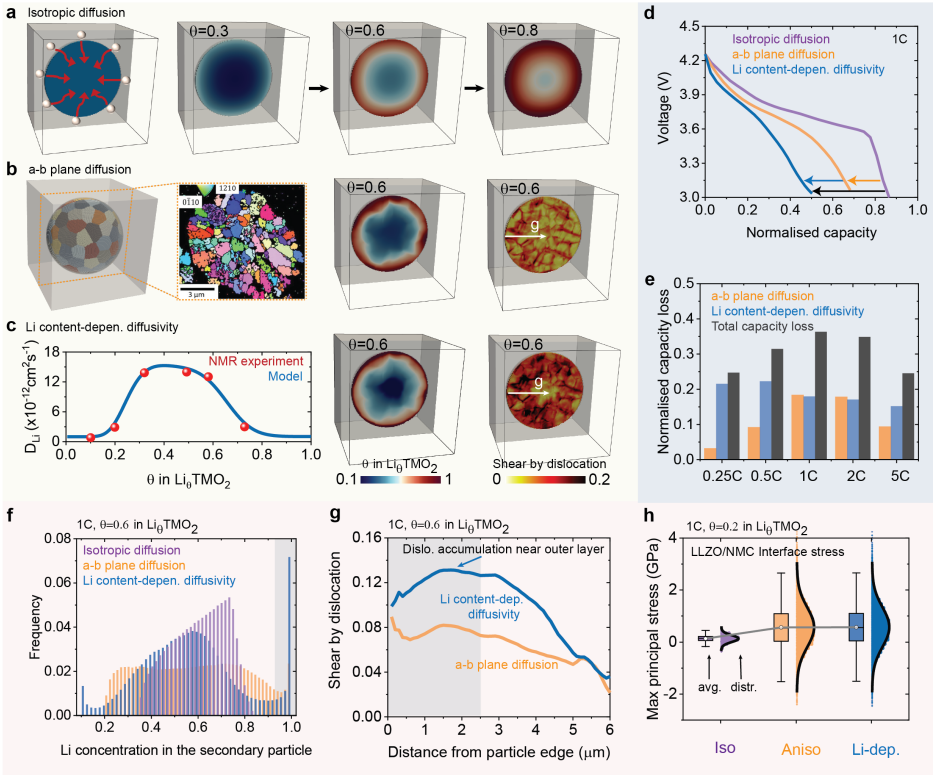

Fig. 3 Effect of crystalline anisotropy and state-of-charge dependent diffusivity in Li-ion dynamics, dislocation formation, interface mechanics, and electrochemical performance. **a-c**, Li concentration maps and dislocation-induced shear distribution (driven by Li-ion intercalation) within the secondary particle at a discharge rate of 1 C, with isotropic Li diffusion (**a**), anisotropic Li diffusion [30] (**b**), and anisotropic Li concentration-dependent diffusion [36, 37] (**c**). **d**, Voltage-capacity profiles under different diffusion scenarios. **e**, Effect of discharge rates on capacity loss. **f**, Li concentration distribution within secondary particles. **g**, The average dislocation-induced shear deformation as a function of distance from the particle edge. **h**, Maximum principle stress distribution at the cathode/solid-electrolyte interface.

(dis)charge to the theoretical capacity within $1/n$ hours). Moreover, the strong sensitivity of diffusivity to Li content exacerbates the situation, further compounding the capacity loss from 15% to 22% over a broad spectrum of discharge rates, from 0.25 C to 5 C. Operando optical microscopy observations also confirm the persistent presence of Li heterogeneities within the cathode particle across a wide range of discharge rates [37, 38].

Fig. 3b,c show that the large anisotropic volume change of Ni-rich layered cathodes driven by Li intercalation and the cathode microstructure heterogeneity result in substantial differences in dislocation activity and accumulation between primary particles. This indicates that even primary particles of identical size and orientation will

exhibit a degree of dislocation activity that highly depends on their location within the agglomerate. Additionally, the sharp drop in Li diffusivity towards higher Li content conditions leads to a pronounced concentration gradient across the secondary particle. This Li heterogeneity can generate a significant difference in lattice dimensions and distortions between the Li-rich and Li-poor domains. Therefore, as shown in Fig. 3g, basal dislocations accumulate prominently near the exterior of the secondary particle. The formation of crystal defects, such as dislocations, will result in high stress build-up and very large local lattice strains. This effect, in turn, modifies the local bonding environment for oxygen, ultimately promoting oxygen deficiency [4, 5, 18–20, 24]. The accumulation of these basal dislocations thus facilitates the structural degradation from the layered structure to the spinel-like phase within the agglomerate's periphery [4, 5]. This structural degradation carries consequences beyond mere active material loss; it hinders the efficient intercalation of Li-ion into the agglomerate's core. Consequently, this exacerbates the kinetics-induced capacity loss, compounding the adverse effects on the composite cathode's performance.

In addition to its influence on Li-ion dynamics and the formation of crystal defects, the crystalline anisotropy of primary particles plays a pivotal role in cathode/solid-electrolyte interface mechanics. Fig. 3h shows the statistical variability in the maximum principle stress distribution on the interface (driving force for contact loss), before and after considering the effect of crystalline anisotropy. The results suggest that while the polycrystalline particle exhibits, on average, 2%-7% volume expansion upon lithiation, most regions within the cathode/solid-electrolyte interface experience substantial tensile stress during discharge. This observation indicates that the potential mechanical failure of the cathode/solid-electrolyte interface is driven by the combination of anisotropic lattice strains and microstructure heterogeneity.

4 Role of microstructure in rate performance and defect heterogeneity

Insights about the spatial dynamics of Li intercalation and the heterogeneous distribution of crystal defect leverage an improved understanding of the rate performance, electrochemical and mechanical degradation mechanisms of solid-state batteries. Here, we investigate the role of secondary particle size and discharge rate on state-of-charge heterogeneities and dislocation activity in single crystal and polycrystalline NMC cathodes. Fig. 4a shows the predicted and experimental voltage-capacity profiles of the polycrystal cathode during galvanostatic discharge tests [39], where the discharge rate is gradually increased from 0.1 C to 2 C. The good agreement between simulations and experiments confirms the effectiveness of the developed physics-based chemo-mechanical model. Furthermore, as shown in Fig. 4b and Supplementary Fig. S.6, 7, for both single crystal and polycrystalline cathodes, the capacity-rate trade-off can be improved by decreasing the secondary particle size of cathodes.

Fig. 4d suggests that both single crystal and polycrystalline cathodes exhibit similar spatial dynamics of lithiation across a broad range of discharge rates, from 0.25 C to 5 C. However, there are significant differences in dislocation activity between single crystalline and polycrystalline cathodes. At a low discharge rate of 0.25 C, we

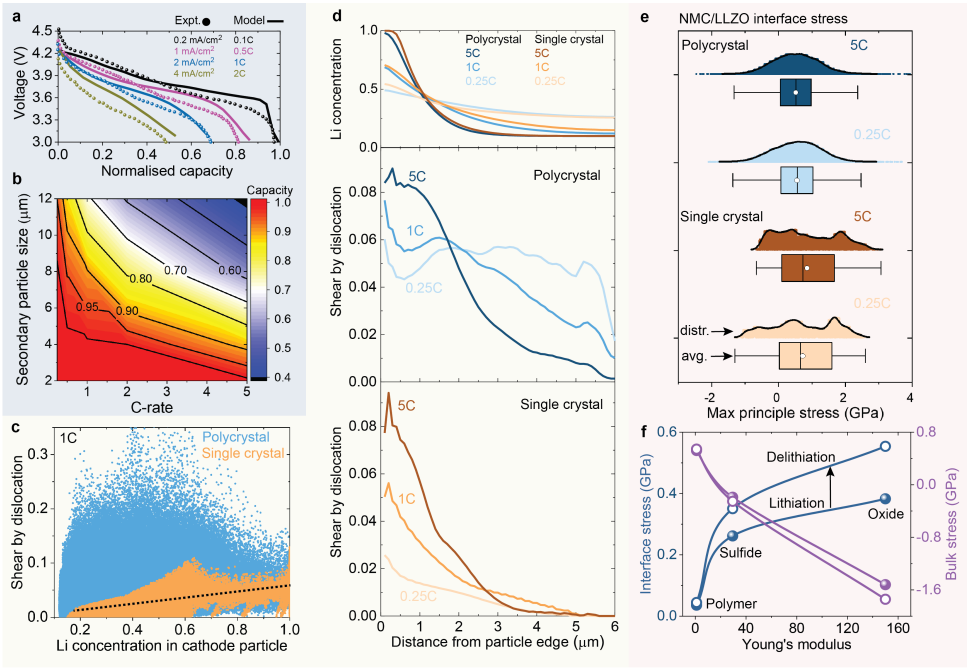

Fig. 4 Effect of cathode microstructure and operating conditions on dislocation heterogeneity and mechanical stability. a, Voltage-capacity profiles at various discharge rates for the polycrystalline cathode with a diameter of 12 μm [39]. **b**, Effect of the secondary particle size and discharge rate on the capacity of polycrystalline composite cathodes. **c**, Correlation between Li concentration and dislocation-induced plastic shear in cathodes. **d**, The average Li concentration and plastic shear within the particle as a function of distance from the particle edge. **e**, Maximum principle stress distribution at the cathode/solid-electrolyte interface. **f**, Effect of the Young's modulus of solid electrolytes on the stress response at the cathode/solid-electrolyte interface and within the cathode particles.

observe a high level of dislocation activity in the polycrystalline particle, while the dislocation activity is relatively low in the single crystal particle. Transitioning a high discharge rate of 5 C, dislocations accumulate at the edge of both polycrystalline and single crystal particles; however, the polycrystalline particle exhibits a much broader defect-rich region. This implies that dislocations primarily form as a result of the Li inhomogeneity-induced strain gradient within single crystal particles under high current density conditions, while both operating conditions and the random arrangement of primary particles in the secondary particle play a critical role in dislocation heterogeneity for polycrystal cathodes. Furthermore, as depicted in Fig. 4c, a positive correlation between the Li concentration and dislocation activity is evident for the single crystal particle, whereas a relatively high dislocation activity is observed in the polycrystalline particle, irrespective of Li content.

Fig. 4e and Supplementary Fig. S.8, 9 show the distribution of the maximum principle stress at the cathode/solid-electrolyte interface, for both single crystal and

polycrystalline particles exposed to various discharge rates. A high tensile stress persists at the interface, irrespective of whether a single crystal or polycrystalline cathode is considered. Moreover, the comparative analysis under different discharge rates in Fig. 4e reveals that the reduction of the discharge rate is not a solution for alleviating this persistent tensile stress at interfaces. However, Fig. 4f shows that reducing the Young's modulus of the solid electrolytes instead, through the utilization of polymer-based or sulfide solid electrolytes, effectively alleviates the high tensile stress at the interface and enhances the overall mechanical stability.

5 Dislocation-induced structural degradation and capacity loss

The presence of crystal defects, such as dislocations and stacking faults, not only induces large lattice strains but also dramatically modifies the local oxygen environment, which manifests itself through inserting extra lattice planes or perturbing the sequence of the oxygen layers [4, 5, 18–20, 24]. Density functional theory (DFT) calculations reveal that the formation energy of the oxygen vacancy can be markedly reduced from 1.06 eV to 0.24 eV with applying a 10% tensile strain to the layered oxide cathode [4]. Moreover, stacking faults and dislocations can provide an alternative route to form different disordered structures by offering a greater freedom to the displacement of TM ions into the alkali metal layers [26, 27]. Dislocation-induced irreversible oxygen release and structural degradation is schematically shown in Fig. 5a (details in Supplementary section S.1.4). This argument is further substantiated by a comprehensive range of characterizations spanning from the atomic to micro-length scale, including HRTEM, Bragg coherent X-ray diffraction imaging (BCDI), and transmission-based X-ray absorption spectromicroscopy and ptychography experiments [4, 5, 20, 26, 40] (Fig. 5b).

In the left panel of Fig. 5b, HRTEM characterization of a layered oxide cathode after charging shows that pronounced lattice displacements can trigger oxygen loss and TM migration, subsequently leading to a phase transition from the layered structure to the spinel phase [4]. In situ BCDI measurements illustrate that tensile strain starts accumulating preferentially near the particle surface region and gradually expands into the interior of the particle (top-right of Fig. 5b) [4], which is also manifested by the predicted distribution of dislocation-induced plastic shear (driven by Li intercalation) in the entire particle after discharge (middle of Fig. 5b). The inhomogeneous Li concentration distribution and the accumulation of crystal defects significantly affect the structural stability of Ni-rich and Li-rich cathodes, which may ultimately trigger the bulk decomposition of these layered phases. The oxidation state maps obtained through X-ray spectromicroscopy and ptychography reveal that oxygen deficiency persists within the bulk of secondary particles, rather than being limited to the near-surface (a few nanometers) region of the particle (bottom-right of Fig. 5b) [5]. Additionally, these quantitative results show that the arrangement of primary particles within secondary particles results in notable heterogeneity in the extent of oxygen loss among the primary particles. This observed heterogeneity in oxygen deficiency aligns with the predicted inhomogeneous distribution of plastic shear-induced oxygen

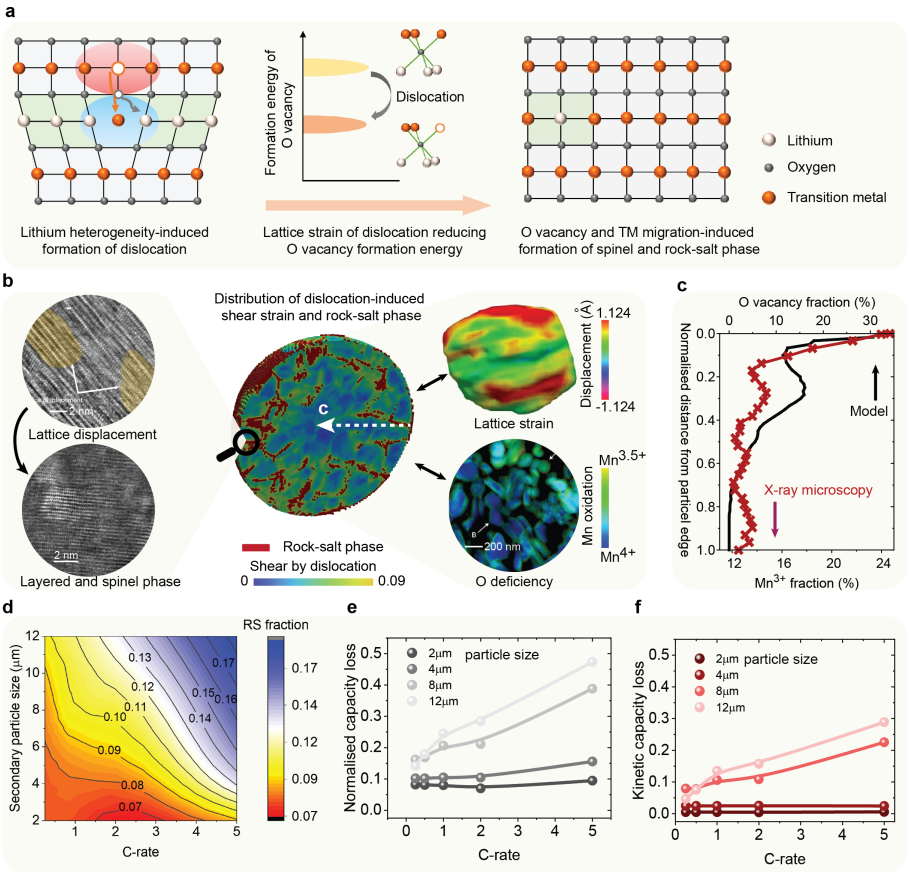

Fig. 5 Dislocation-induced structural degradation and capacity loss. a, Schematic of dislocation-induced irreversible oxygen release and structural degradation. Dislocations induce large lattice strain and dramatically modify the local oxygen environment, which can markedly impact the structural stability of the layered phase and trigger oxygen loss and TM migration. **b**, HRTEM images of lattice displacement and phase transition [4] (left); predicted distribution of dislocation-induced plastic shear and oxygen-deficient phase (middle); lattice strains obtained by BCDI measurements [4] (top-right); X-ray ptychography image of the Mn oxidation state [5] (bottom-right). **c**, Comparison of the predicted and measured oxygen deficiency. **d**, Effect of particle size and discharge rate on the fraction of oxygen-deficient phase. **e**, Total capacity loss after accounting for the irreversible phase transition, as a function of the particle size and discharge rate. **f**, Kinetics-induced capacity loss arising from the impediment of Li-ion intercalation pathways.

loss within the secondary particle, as shown in the middle of Fig. 5b. Despite the spatial variation in oxygen deficiency, both experiments [5] and predictions depicted in Fig. 5c consistently indicate that, on average, primary particles located near the exterior of the agglomerate are more susceptible to oxygen loss compared to those in the interior.

Fig. 5d shows the effect of the secondary particle size and discharge rate on the fraction of the oxygen-deficient phase within the secondary particle. The results demonstrate that in secondary particles larger than approximately 8 μm, significant

bulk structural degradation occurs when these particles are subjected to the discharge rates exceeding 1 C, leading to a loss of over 10% of active materials. This emphasizes the critical impact of both cathode microstructure and operating conditions on the overall quantity and distribution of the oxygen-deficient phase, a factor that can significantly affect the electrochemical performance of composite cathodes. Fig. 5e shows the predicted capacity loss of composite cathodes after accounting for the irreversible oxygen-deficient phase transition in cathodes, as a function of the secondary particle size and discharge rate. A noticeable difference in behaviour is observed: particles exceeding 8 μm in diameter tend to exhibit a significant capacity loss, ranging from 20% to 40%, as the discharge rate increases from 1 C to 5 C, while this effect is less pronounced for smaller particles. This phase transition-induced capacity loss is attributed to a combination of factors, including the loss of active materials (thermodynamic effect) and the impediment of Li-ion intercalation pathways within the cathodes (kinetic effect). Furthermore, Fig. 5f shows that secondary particles exceeding 8 μm in diameter and subjected to discharge rates greater than 1 C experience a kinetics-induced capacity loss of over 10%, which is primarily attributed to the accumulation of crystal defects and associated structural degradation at the particle's periphery.

6 Implications for capacity loss mitigation

The pursuit of mitigating capacity loss in Ni-rich oxide cathodes has been a focal point of research, targeting challenges including oxygen loss, structural degradation, and mechanical failure within composite electrodes [1–3, 6, 7, 9, 12, 16]. To date, surface coating and modification stand out as the predominant methodologies for curbing undesirable side reactions between oxide cathodes and solid electrolytes [13–15]. While irreversible surface degradation plays a role in capacity loss, the significant hurdle arises from crystal defect-induced phase transitions from the layered structure to the spinel-like phase within the interior of cathode particles, posing a formidable barrier to the practical implementation of Ni-rich and Li-rich cathodes [4, 5, 16, 17, 28]. In light of this, it becomes imperative to explore additional approaches that can complement established surface engineering methods.

Addressing crystal defects and lattice strain challenges in Ni-rich cathodes necessitates a holistic consideration of the heterogeneous cathode microstructure and large anisotropic volume changes driven by Li mass transport. This calls for a fundamental consideration of composition design and microstructure regulation. Our findings underscore the potential of morphological optimization and a controlled rate of Li (de)intercalation as chemistry-agnostic strategies to enhance stability against oxygen loss. As shown in Fig. 6a,b, strategies including reducing the secondary particle diameter to below 4 μm and employing single crystal layered cathodes devoid of interparticle boundaries have proven effective in mitigating the capacity fading issue observed in conventional polycrystalline cathodes [6, 41]. Reducing the diameter of secondary particles from 9 μm to below 4 μm enables the increase of the discharge rate from 1 C to 5 C while maintaining the same 90% usable capacity. This improvement is attributed to the effective shortening of the Li intercalation path and a reduced accumulation of crystalline defects, such as dislocations, during battery operation. Fig. 6c shows

that using a single type of solid electrolytes cannot simultaneously mitigate the large tensile stress buildup in NMC cathodes and on the interfaces between these cathodes and the solid electrolytes. This often leads to either the formation of intergranular cracks within the cathodes or contact loss along the cathode/solid-electrolyte interfaces. Therefore, hybrid systems that involve both oxides and polymer electrolytes seem to be a promising solution to address the mechanical degradation issues in solid state batteries [1]. Furthermore, preventing cation disordering emerges as a potent means to inhibit the structural changes required to accommodate oxygen vacancies. For instance, the ribbon superstructure, as opposed to the honeycomb superstructure in TM metal layers within sodium-ion intercalation cathodes proves capable of suppressing manganese disorder and the associated oxygen molecule formation, during the P2 to O2 phase transition involving slab gliding [28, 42, 43].

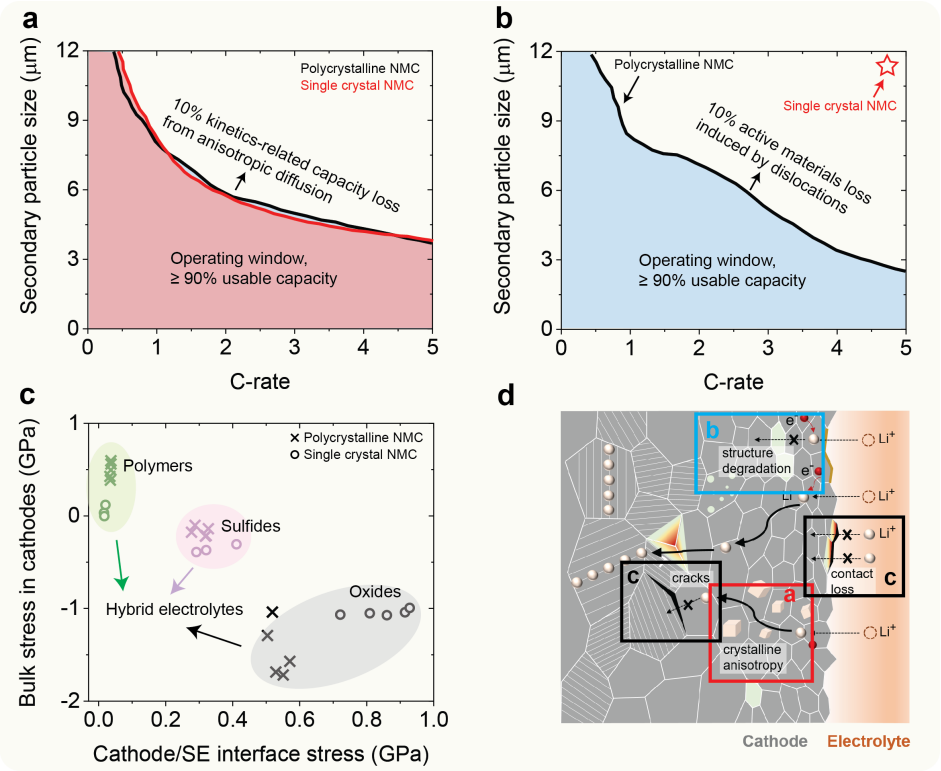

Fig. 6 Microstructural effects in solid-state cathode composites. **a**, Contours of 10% kinetics-related capacity loss due to the anisotropic Li diffusion as a function of particle diameter and C-rate. **b**, Contours of 10% loss of active materials induced by the formation of dislocations as a function of particle diameter and C-rate. **c**, Relationships between the bulk stress within NMC cathodes and the interface stress (maximum tensile stress) between cathodes and the solid electrolytes. Different points correspond to the results under various discharge rates from 0.25 C to 5 C. **d**, Schematic view of different chemo-mechanical degradation mechanisms: anisotropic diffusion-induced capacity loss; structural degradation induced by dislocations; crack formation and contact loss.

The large anisotropic volume changes of Ni-rich cathode materials during cycling result in the mechanical degradation at the cathode/solid-electrolyte interface, which leads to the increase of electrode impedance and capacity loss [44]. This phenomenon is compounded by the substantial formation of crystal defects within the cathode particles, to reduce the stress magnitude and accommodate the large compositional strain. First-principle calculations suggest that transition-metal centres with non-bonding electronic configurations, cation disordering, redox-inactive species, isotropic structures, and octahedral-to-tetrahedral migration of Li can effectively minimize volume changes upon (dis)charging [45]. For instance, the introduction of compositionally complex dopants (Ti, Mg, Nb, and Mo) to Ni-rich layered cathodes or the incorporation of a coherent perovskite phase into the layered structure demonstrates a marked reduction in lattice dimension changes over a wide electrochemical window [46, 47]. This approach effectively mitigates the structural degradation through a pinning effect. Furthermore, eliminating synthesis-induced crystal defects, such as low-angle tilt boundaries, anti-phase boundaries, stacking faults, and dislocations, contributes to superior structural stability at high voltages while preventing irreversible oxygen release [48, 49].

7 Conclusions

In conclusion, our study presents and applies a meso-scale chemo-mechanical constitutive model for investigating the effect of grain-level chemo-mechanics on the electrochemical performance and degradation mechanisms in composite cathodes of solid-state batteries. Integrating multi-scale experimental and theoretical findings, we reveal that Ni-rich cathodes experience extensive dislocation formation (over 12% plastic shear locally) during discharge, due to the large compositional strains, crystalline anisotropy, and non-equilibrium Li-ion intercalation dynamics. Anisotropic diffusion within the a-b plane, coupled with the high Li diffusivity sensitivity to Li content, lead to the heterogeneous Li distribution within cathodes, causing a marked increase in over-potential and capacity loss. Accumulated dislocations on the cathode periphery induce large lattice strain and profoundly alter the local oxygen environment, potentially triggering oxygen release and the displacement of transition metal ions into the alkali metal layers. The formation of crystal defects in the bulk of cathode particles driven by Li intercalation can not be alleviated by the established surface coating and modification approaches. Strategies such as reducing the secondary particle diameter to below 4 μm, using single crystal cathodes without interparticle boundaries, and compositionally complex doping, prove effective in countering the generation of crystal defects and addressing capacity fading in conventional polycrystalline cathodes. The results also imply that contact loss at the cathode/solid-electrolyte interface is intricately linked to the anisotropic volume change during Li (de)intercalation and the mechanical properties of solid electrolytes. Reduction in current densities proves insufficient to alleviate the persistent tensile stress and contact loss at the interface. This work provides insights into the role of the crystalline anisotropy and grain-level

chemo-mechanics in crystal defect generation and mechanical degradation mechanisms of composite electrodes with Ni-rich cathodes, offering valuable contributions to improving energy storage system design.

8 Methods

8.1 Governing equations

The free energy of the NMC811 cathode can be described variationally as including the chemical free energy and mechanical energy within the finite-strain framework,

$$\mathcal{F}(c,\mathbf{F}) = \int_V \Big(f_{\text{chem}}(c) + f_{\text{mech}}(c,\mathbf{F}) \Big) \mathrm{d}V, \tag{1}$$

where V is the domain of consideration, f_{chem} and f_{mech} describe the bulk chemical and mechanical energy density, respectively. c is the Li fraction ($0 \leq c \leq 1$, the fraction of lattice sites occupied by Li). $\mathbf{F}$ is the total deformation gradient.

Li reaction at the cathode/solid-electrolyte interface and diffusion within the cathode are modelled by the Cahn-Hilliard reaction-diffusion equation [31, 33],

$$\frac{\partial c}{\partial t} = -\nabla \cdot \mathbf{j} + R(c,\mu,\eta), \tag{2}$$

in which t is time, $\mathbf{j}$ is the corresponding Li-ion flux density, and R is the reaction rate depending on the local state-of-charge and the overpotential η.

Since the relaxation time for mechanical deformation is fast for solids compared to reaction-diffusion of Li-ion, we assume mechanical equilibrium at all times,

$$\nabla \cdot \mathbf{P} = \mathbf{0}, \tag{3}$$

where the left-hand side is the divergence of the first Piola-Kirchhoff stress $\mathbf{P}$.

8.2 Reaction-diffusion model

The interface reaction is described by a boundary condition expressing mass conservation on the reactive surfaces,

$$R = -\mathbf{n} \cdot \mathbf{j}, \tag{4}$$

where $\mathbf{j}$ is the diffusive flux on the surface, and $\mathbf{n}$ is the unit normal to the reactive surface. The reaction rate depends on the local state-of-charge and the local overpotential, which can be described via generalized Butler-Volmer kinetics [31]. In this study, galvanostatic simulations are performed for a given discharge rate. Consequently, a constant ionic flux $\mathbf{j}$ is applied normal to the reactive surface of the secondary particle and is directly related to the current density.

The regular solution model is used to model the homogeneous chemical free energy,

$$\Omega f_{\text{chem}}(c) = k_{\text{B}}T\big(c\,\ln c + (1-c)\ln(1-c)\big) + E_1 c + E_{11} c^2 \tag{5}$$

where Ω is the molar volume; k_B is the universal gas constant; E_1 and E_{11} are material coefficients that can obtained from the open circuit voltage of a NMC half-cell [36].

The flux force for Li-ion diffusion is described by

$$\mathbf{j} = -\mathbf{M} \cdot \nabla \mu, \tag{6}$$

where $\mathbf{M}$ is the anisotropic mobility tensor, and μ is Li chemical potential. Lithium intercalation in the cathode is driven by the gradient of the Li chemical potential μ. The chemical potential of Li in NMC cathode is defined as the variational derivative of the total free energy to Li concentration

$$\mu = \frac{\delta \mathcal{F}}{\delta c}. \tag{7}$$

8.3 Mechanical constitutive model

The finite-strain deformation field $\boldsymbol{\chi}(\mathbf{x}) : \mathbf{x} \in \mathcal{B}_0 \rightarrow \mathbf{y} \in \mathcal{B}$ maps material points $\mathbf{x}$ in the reference configuration $\mathcal{B}_0$ to points $\mathbf{y}$ in its deformed configuration $\mathcal{B}$. The total deformation gradient is defined as

$$\mathbf{F} = \frac{\partial \boldsymbol{\chi}}{\partial \mathbf{x}} = \nabla \boldsymbol{\chi}. \tag{8}$$

In the current study, the deformation gradient $\mathbf{F}$ is multiplicatively decomposed as

$$\mathbf{F} = \mathbf{F}_e \mathbf{F}_c \mathbf{F}_p, \tag{9}$$

in terms of the elastic strain $\mathbf{F}_e$, dislocation-induced plastic strain $\mathbf{F}_p$, and compositional eigenstrain $\mathbf{F}_c$ [33, 35, 50]. The compositional eigenstrain $\mathbf{F}_c$ is Li-ion concentration dependent and links the relation between the local state-of-charge and lattice mismatch in the a, b and c directions, respectively. The plastic deformation gradient $\mathbf{F}_p$ is incorporated to depict the accumulation of plastic shear arising from $a-b$ plane dislocations within cathodes.

The local deformation arising from Li-ion (de)intercalation is given by

$$\mathbf{F}_c = \mathbf{I} + \mathbf{V}_c. \tag{10}$$

The components of $\mathbf{V}_c$ can be expressed as:

$$\mathbf{V}_c = \begin{bmatrix} \nu^a & 0 & 0 \\ 0 & \nu^b & 0 \\ 0 & 0 & \nu^c \end{bmatrix}, \tag{11}$$

in the crystal's coordinate system. The (de)lithiation strain $\mathbf{F}_c$ is determined as a function of Li concentration through the experimentally measured lattice parameter changes along different crystallographic directions [51].

The evolution of plastic deformation gradient $\mathbf{F}_\mathrm{p}$ is given in terms of the plastic velocity gradient $\mathbf{L}_\mathrm{p}$ by the flow rule

$$\dot{\mathbf{F}_\mathrm{p}} = \mathbf{L}_\mathrm{p}\mathbf{F}_\mathrm{p}. \tag{12}$$

To describe the dislocation slip on the $a-b$ plane, a crystal plasticity model [35, 50, 52] is used, where the plastic velocity gradient $\mathbf{L}_\mathrm{p}$ consists of the slip rates $\dot{\gamma}^\alpha$ on crystallographic slip systems,

$$\mathbf{L}_\mathrm{p} = \sum_\alpha \dot{\gamma}^\alpha \mathbf{m}^\alpha \otimes \mathbf{n}^\alpha, \tag{13}$$

where $\dot{\gamma}^\alpha$ denotes the shear rate on slip system α, and vectors $\mathbf{m}^\alpha$ and $\mathbf{n}^\alpha$ are the slip direction and slip plane normal of slip systems, respectively. The shear rate is given in terms of the phenomenological description as

$$\dot{\gamma}^\alpha = \dot{\gamma}_0 \left| \frac{\tau^\alpha}{g^\alpha} \right|^n \mathrm{sgn}(\tau^\alpha), \tag{14}$$

where $\dot{\gamma}_0$ is the reference shear rate, τ^α is the resolved shear stress on slip system α, n is the strain-rate sensitivity exponent. The slip resistance g^α evolves from its initial value (g_0) asymptotically to a system-dependent saturation value g_∞ and depends on shear on slip systems ($\gamma^\beta, \beta = 1, 2, 3$) according to the relationship

$$\dot{g}^\alpha = \dot{\gamma}^\beta \, h_0 \left| 1 - g^\beta / g_\infty \right|^a \mathrm{sgn}(1 - g^\beta / g_\infty) h_{\alpha\beta}, \tag{15}$$

with hardening parameters h_0, a, and $h_{\alpha\beta}$.

The mechanical energy density, f_mech is modelled by the following form

$$f_\mathrm{mech} = \frac{1}{2}\mathbf{E}_\mathrm{e} \cdot \mathbb{C}\mathbf{E}_\mathrm{e}, \tag{16}$$

where $\mathbb{C}$ is the anisotropic elastic stiffness. $\mathbf{E}_\mathrm{e}$ is the Green-Lagrange strain, which is calculated as

$$\mathbf{E}_\mathrm{e} = \frac{1}{2}\mathbf{F}_\mathrm{c}^\mathrm{T}(\mathbf{F}_\mathrm{e}^\mathrm{T}\mathbf{F}_\mathrm{e} - \mathbf{I})\mathbf{F}_\mathrm{c}, \tag{17}$$

The work conjugate second Piola-Kirchhoff stress $\mathbf{S}$ is given by,

$$\mathbf{S} = \mathbb{C}\mathbf{E}_\mathrm{e}, \tag{18}$$

which is related to the first Piola-Kirchhoff stress $\mathbf{P}$ through

$$\mathbf{P} = \mathbf{F}_\mathrm{e}\mathbf{F}_\mathrm{c}\mathbf{S}\mathbf{F}_\mathrm{p}^{-\mathrm{T}}. \tag{19}$$

8.4 Oxygen vacancy formation energy

The formation of crystal defects, such as dislocations, not only leads to large lattice strain but also dramatically modifies the local oxygen environment, which manifests through inserting extra lattice planes or perturbing the sequence of oxygen layers [4, 5, 19, 20]. The role of lattice strain arsing from dislocations in the formation energy of oxygen vacancies in the layered oxide structure is assessed via atomic-scale calculations [4, 20, 26, 27]. The formation energy of oxygen vacancy (E_{O}) is given by the following equation:

$$E_{\mathrm{O}}[\mathrm{V_O}] = E_{\mathrm{total}}[\mathrm{V_O}] - E_{\mathrm{total}}[\mathrm{P}] + \mu_{\mathrm{O}}, \tag{20}$$

where $E_{\mathrm{total}}[\mathrm{V_O}]$ and $E_{\mathrm{total}}[\mathrm{P}]$ denote the total energy of the supercells with and without an oxygen vacancy, respectively. μ_{O} is the chemical potential of oxygen, where the gas phase O_2 molecule is used as the reference state. The details of these first principle calculations can be found in the references [4, 20, 26, 27]. Supplementary Fig. S.4 shows the influence of the applied tensile strain on the formation energy of oxygen vacancy in the layered oxide structure. The results indicate that the increased lattice strain notably decreases the energy barrier to remove lattice oxygen [4]. To account for the impact of dislocation-induced shear during Li (de)intercalation on oxygen release in our meso-scale chemo-mechanical simulations, the material domains with a plastic shear exceeding 12% are delineated as the oxygen-deficient phase.

Declarations

The authors declare no competing interests.

References

[1] Janek, J., Zeier, W.G.: Challenges in speeding up solid-state battery development. Nature Energy **8**(3), 230–240 (2023)

[2] Kalnaus, S., Dudney, N.J., Westover, A.S., Herbert, E., Hackney, S.: Solid-state batteries: The critical role of mechanics. Science **381**(6664), 5998 (2023)

[3] Bartsch, T., Strauss, F., Hatsukade, T., Schiele, A., Kim, A.-Y., Hartmann, P., Janek, J., Brezesinski, T.: Gas evolution in all-solid-state battery cells. ACS Energy Letters **3**(10), 2539–2543 (2018)

[4] Liu, T., Liu, J., Li, L., Yu, L., Diao, J., Zhou, T., Li, S., Dai, A., Zhao, W., Xu, S., *et al.*: Origin of structural degradation in Li-rich layered oxide cathode. Nature **606**(7913), 305–312 (2022)

[5] Csernica, P.M., Kalirai, S.S., Gent, W.E., Lim, K., Yu, Y.-S., Liu, Y., Ahn, S.-J., Kaeli, E., Xu, X., Stone, K.H., *et al.*: Persistent and partially mobile oxygen vacancies in Li-rich layered oxides. Nature Energy **6**(6), 642–652 (2021)

[6] Bi, Y., Tao, J., Wu, Y., Li, L., Xu, Y., Hu, E., Wu, B., Hu, J., Wang, C., Zhang, J.-G., *et al.*: Reversible planar gliding and microcracking in a single-crystalline Ni-rich cathode. Science **370**(6522), 1313–1317 (2020)

[7] Koerver, R., Aygün, I., Leichtweiß, T., Dietrich, C., Zhang, W., Binder, J.O., Hartmann, P., Zeier, W.G., Janek, J.: Capacity fade in solid-state batteries: interphase formation and chemomechanical processes in nickel-rich layered oxide cathodes and lithium thiophosphate solid electrolytes. Chemistry of Materials **29**(13), 5574–5582 (2017)

[8] Xu, C., Märker, K., Lee, J., Mahadevegowda, A., Reeves, P.J., Day, S.J., Groh, M.F., Emge, S.P., Ducati, C., Layla Mehdi, B., *et al.*: Bulk fatigue induced by surface reconstruction in layered Ni-rich cathodes for Li-ion batteries. Nature Materials **20**(1), 84–92 (2021)

[9] Banerjee, A., Wang, X., Fang, C., Wu, E.A., Meng, Y.S.: Interfaces and interphases in all-solid-state batteries with inorganic solid electrolytes. Chemical Reviews **120**(14), 6878–6933 (2020)

[10] Koerver, R., Walther, F., Aygün, I., Sann, J., Dietrich, C., Zeier, W.G., Janek, J.: Redox-active cathode interphases in solid-state batteries. Journal of Materials Chemistry A **5**(43), 22750–22760 (2017)

[11] Shin, H.-J., Kim, J.T., Kim, A.-Y., Noh, N., Park, J., Park, C.R., Yu, S., Kim, H., Chung, K.Y., Yuk, J.M., et al.: New consideration of degradation accelerating of all-solid-state batteries under a low-pressure condition. Advanced Energy Materials, 2301220 (2023)

[12] Dong, Y., Li, J.: Oxide cathodes: functions, instabilities, self healing, and degradation mitigations. Chemical Reviews **123**(2), 811–833 (2022)

[13] Culver, S.P., Koerver, R., Zeier, W.G., Janek, J.: On the functionality of coatings for cathode active materials in thiophosphate-based all-solid-state batteries. Advanced Energy Materials **9**(24), 1900626 (2019)

[14] Liang, J., Zhu, Y., Li, X., Luo, J., Deng, S., Zhao, Y., Sun, Y., Wu, D., Hu, Y., Li, W., *et al.*: A gradient oxy-thiophosphate-coated Ni-rich layered oxide cathode for stable all-solid-state Li-ion batteries. Nature Communications **14**(1), 146 (2023)

[15] Wan, H., Wang, Z., Zhang, W., He, X., Wang, C.: Interface design for all-solid-state lithium batteries. Nature, 1–6 (2023)

[16] Zhang, H., Liu, H., Piper, L.F., Whittingham, M.S., Zhou, G.: Oxygen loss in layered oxide cathodes for Li-ion batteries: mechanisms, effects, and mitigation. Chemical Reviews **122**(6), 5641–5681 (2022)

[17] Wang, Z., Wang, Z., Xue, D., Zhao, J., Zhang, X., Geng, L., Li, Y., Du, C., Yao,

J., Liu, X., *et al.*: Reviving the rock-salt phases in Ni-rich layered cathodes by mechano-electrochemistry in all-solid-state batteries. Nano Energy **105**, 108016 (2023)

[18] Li, S., Yao, Z., Zheng, J., Fu, M., Cen, J., Hwang, S., Jin, H., Orlov, A., Gu, L., Wang, S., *et al.*: Direct observation of defect-aided structural evolution in a nickel-rich layered cathode. Angewandte Chemie International Edition **59**(49), 22092–22099 (2020)

[19] Ulvestad, A., Singer, A., Clark, J., Cho, H., Kim, J.W., Harder, R., Maser, J., Meng, Y., Shpyrko, O.: Topological defect dynamics in operando battery nanoparticles. Science **348**(6241), 1344–1347 (2015)

[20] Singer, A., Zhang, M., Hy, S., Cela, D., Fang, C., Wynn, T., Qiu, B., Xia, Y., Liu, Z., Ulvestad, A., *et al.*: Nucleation of dislocations and their dynamics in layered oxide cathode materials during battery charging. Nature Energy **3**(8), 641–647 (2018)

[21] Gorobtsov, O.Y., Hirsh, H., Zhang, M., Sheyfer, D., Nguyen, L.H.B., Matson, S.D., Weinstock, D., Bouck, R., Wang, Z., Cha, W., et al.: Operando interaction and transformation of metastable defects in layered oxides for Na-ion batteries. Advanced Energy Materials, 2203654 (2023)

[22] Han, M., Liu, Z., Shen, X., Yang, L., Shen, X., Zhang, Q., Liu, X., Wang, J., Lin, H.-J., Chen, C.-T., *et al.*: Stacking faults hinder lithium insertion in Li_2RuO_3. Advanced Energy Materials **10**(48), 2002631 (2020)

[23] Xu, Z., Hou, D., Kautz, D.J., Liu, W., Xu, R., Xiao, X., Lin, F.: Charging reactions promoted by geometrically necessary dislocations in battery materials revealed by in situ single-particle synchrotron measurements. Advanced Materials **32**(37), 2003417 (2020)

[24] Gong, Y., Chen, Y., Zhang, Q., Meng, F., Shi, J.-A., Liu, X., Liu, X., Zhang, J., Wang, H., Wang, J., *et al.*: Three-dimensional atomic-scale observation of structural evolution of cathode material in a working all-solid-state battery. Nature Communications **9**(1), 3341 (2018)

[25] Yan, P., Zheng, J., Chen, T., Luo, L., Jiang, Y., Wang, K., Sui, M., Zhang, J.-G., Zhang, S., Wang, C.: Coupling of electrochemically triggered thermal and mechanical effects to aggravate failure in a layered cathode. Nature Communications **9**(1), 2437 (2018)

[26] Li, Q., Yao, Z., Lee, E., Xu, Y., Thackeray, M.M., Wolverton, C., Dravid, V.P., Wu, J.: Dynamic imaging of crystalline defects in lithium-manganese oxide electrodes during electrochemical activation to high voltage. Nature Communications **10**(1), 1692 (2019)

[27] Song, J.-H., Yu, S., Kim, B., Eum, D., Cho, J., Jang, H.-Y., Park, S.-O., Yoo, J., Ko, Y., Lee, K., *et al.*: Slab gliding, a hidden factor that induces irreversibility and redox asymmetry of lithium-rich layered oxide cathodes. Nature Communications **14**(1), 4149 (2023)

[28] House, R.A., Rees, G.J., Pérez-Osorio, M.A., Marie, J.-J., Boivin, E., Robertson, A.W., Nag, A., Garcia-Fernandez, M., Zhou, K.-J., Bruce, P.G.: First-cycle voltage hysteresis in Li-rich 3*d* cathodes associated with molecular O_2 trapped in the bulk. Nature Energy **5**(10), 777–785 (2020)

[29] Ahmed, S., Pokle, A., Bianchini, M., Schweidler, S., Beyer, A., Brezesinski, T., Janek, J., Volz, K.: Understanding the formation of antiphase boundaries in layered oxide cathode materials and their evolution upon electrochemical cycling. Matter **4**(12), 3953–3966 (2021)

[30] Tanim, T.R., Yang, Z., Finegan, D.P., Chinnam, P.R., Lin, Y., Weddle, P.J., Bloom, I., Colclasure, A.M., Dufek, E.J., Wen, J., *et al.*: A comprehensive understanding of the aging effects of extreme fast charging on high Ni NMC cathode. Advanced Energy Materials **12**(22), 2103712 (2022)

[31] Bazant, M.Z.: Theory of chemical kinetics and charge transfer based on nonequilibrium thermodynamics. Accounts of Chemical Research **46**(5), 1144–1160 (2013)

[32] Zhao, H., Deng, H.D., Cohen, A.E., Lim, J., Li, Y., Fraggedakis, D., Jiang, B., Storey, B.D., Chueh, W.C., Braatz, R.D., *et al.*: Learning heterogeneous reaction kinetics from X-ray videos pixel by pixel. Nature **621**(7978), 289–294 (2023)

[33] Shanthraj, P., Liu, C., Akbarian, A., Svendsen, B., Raabe, D.: Multi-component chemo-mechanics based on transport relations for the chemical potential. Computer Methods in Applied Mechanics and Engineering **365**, 113029 (2020)

[34] Roters, F., Eisenlohr, P., Hantcherli, L., Tjahjanto, D.D., Bieler, T.R., Raabe, D.: Overview of constitutive laws, kinematics, homogenization and multiscale methods in crystal plasticity finite-element modeling: Theory, experiments, applications. Acta materialia **58**(4), 1152–1211 (2010)

[35] Liu, C., Shanthraj, P., Diehl, M., Roters, F., Dong, S., Dong, J., Ding, W., Raabe, D.: An integrated crystal plasticity–phase field model for spatially resolved twin nucleation, propagation, and growth in hexagonal materials. International Journal of Plasticity **106**, 203–227 (2018)

[36] Marker, K., Reeves, P.J., Xu, C., Griffith, K.J., Grey, C.P.: Evolution of structure and lithium dynamics in $LiNi_{0.8}Mn_{0.1}Co_{0.1}O_2$ (NMC811) cathodes during electrochemical cycling. Chemistry of Materials **31**(7), 2545–2554 (2019)

[37] Xu, C., Merryweather, A.J., Pandurangi, S.S., Lun, Z., Hall, D.S., Deshpande,

V.S., Fleck, N.A., Schnedermann, C., Rao, A., Grey, C.P.: Operando visualization of kinetically induced lithium heterogeneities in single-particle layered Ni-rich cathodes. Joule **6**(11), 2535–2546 (2022)

[38] Merryweather, A.J., Schnedermann, C., Jacquet, Q., Grey, C.P., Rao, A.: Operando optical tracking of single-particle ion dynamics in batteries. Nature **594**(7864), 522–528 (2021)

[39] Tan, D.H., Chen, Y.-T., Yang, H., Bao, W., Sreenarayanan, B., Doux, J.-M., Li, W., Lu, B., Ham, S.-Y., Sayahpour, B., *et al.*: Carbon-free high-loading silicon anodes enabled by sulfide solid electrolytes. Science **373**(6562), 1494–1499 (2021)

[40] Sadowski, M., Koch, L., Albe, K., Sicolo, S.: Planar gliding and vacancy condensation: the role of dislocations in the chemomechanical degradation of layered transition-metal oxides. Chemistry of Materials **35**(2), 584–594 (2022)

[41] Strauss, F., Bartsch, T., Biasi, L., Kim, A.-Y., Janek, J., Hartmann, P., Brezesinski, T.: Impact of cathode material particle size on the capacity of bulk-type all-solid-state batteries. ACS Energy Letters **3**(4), 992–996 (2018)

[42] Maitra, U., House, R.A., Somerville, J.W., Tapia-Ruiz, N., Lozano, J.G., Guerrini, N., Hao, R., Luo, K., Jin, L., Pérez-Osorio, M.A., *et al.*: Oxygen redox chemistry without excess alkali-metal ions in $Na_{2/3}[Mg_{0.28}Mn_{0.72}]O_2$. Nature Chemistry **10**(3), 288–295 (2018)

[43] House, R.A., Maitra, U., Pérez-Osorio, M.A., Lozano, J.G., Jin, L., Somerville, J.W., Duda, L.C., Nag, A., Walters, A., Zhou, K.-J., *et al.*: Superstructure control of first-cycle voltage hysteresis in oxygen-redox cathodes. Nature **577**(7791), 502–508 (2020)

[44] Stallard, J.C., Wheatcroft, L., Booth, S.G., Boston, R., Corr, S.A., De Volder, M.F., Inkson, B.J., Fleck, N.A.: Mechanical properties of cathode materials for lithium-ion batteries. Joule (2022)

[45] Zhao, X., Tian, Y., Lun, Z., Cai, Z., Chen, T., Ouyang, B., Ceder, G.: Design principles for zero-strain Li-ion cathodes. Joule **6**(7), 1654–1671 (2022)

[46] Zhang, R., Wang, C., Zou, P., Lin, R., Ma, L., Yin, L., Li, T., Xu, W., Jia, H., Li, Q., *et al.*: Compositionally complex doping for zero-strain zero-cobalt layered cathodes. Nature **610**(7930), 67–73 (2022)

[47] Wang, L., Liu, T., Wu, T., Lu, J.: Strain-retardant coherent perovskite phase stabilized Ni-rich cathode. Nature **611**(7934), 61–67 (2022)

[48] Xu, G.-L., Liu, X., Zhou, X., Zhao, C., Hwang, I., Daali, A., Yang, Z., Ren, Y., Sun, C.-J., Chen, Z., *et al.*: Native lattice strain induced structural earthquake in sodium layered oxide cathodes. Nature Communications **13**(1), 436 (2022)

[49] Liu, X., Xu, G.-L., Kolluru, V.S.C., Zhao, C., Li, Q., Zhou, X., Liu, Y., Yin, L., Zhuo, Z., Daali, A., *et al.*: Origin and regulation of oxygen redox instability in high-voltage battery cathodes. Nature Energy **7**(9), 808–817 (2022)

[50] Liu, C., Roters, F., Raabe, D.: Finite strain crystal plasticity-phase field modeling of twin, dislocation, and grain boundary interaction in hexagonal materials. Acta Materialia **242**, 118444 (2023)

[51] Xu, C., Reeves, P.J., Jacquet, Q., Grey, C.P.: Phase behavior during electrochemical cycling of Ni-rich cathode materials for Li-ion batteries. Advanced Energy Materials **11**(7), 2003404 (2021)

[52] Roters, F., Diehl, M., Shanthraj, P., Eisenlohr, P., Reuber, C., Wong, S.L., Maiti, T., Ebrahimi, A., Hochrainer, T., Fabritius, H.-O., *et al.*: DAMASK–The Düsseldorf Advanced Material Simulation Kit for modeling multi-physics crystal plasticity, thermal, and damage phenomena from the single crystal up to the component scale. Computational Materials Science **158**, 420–478 (2019)